

Deconvolution of adaptive optics images: from theory to practice

Jean-Marc Conan¹, Thierry Fusco¹, Laurent M. Mugnier¹,
Franck Marchis², Claude Roddier³ and François Roddier³

¹ ONERA, DOTA, B.P. 72, 92322 Châtillon Cedex, France ({name}@onera.fr)

² ESO-La Silla, Casilla 19001, Santiago 19, Chile (fmarchis@eso.org)

³ Institute for Astronomy, University of Hawaii, USA (croddier@ifa.hawaii.edu)

ABSTRACT

Practical guidelines are proposed for deconvolution of partially adaptive optics corrected images: from raw data to high photometric precision object restoration. Preliminary processing is discussed (detector calibration, background subtraction...). The deconvolution scheme itself is then presented. It takes into account the noise statistics in the image, the imprecise knowledge of the point spread function (PSF), and the available *a priori* information on the object (spatial structure, positivity...). This deconvolution scheme is first validated on simulated images of NAOS, the AO system of the VLT and then applied to astronomical images. In particular, an edge preserving regularization is tested on several solar system objects: Io, Uranus and Neptune.

Keywords: adaptive optics, atmospheric turbulence, deconvolution, image restoration, inverse problems, astronomy.

1. INTRODUCTION

The performance of high resolution imaging with large astronomical telescopes is severely limited by the atmospheric turbulence. Adaptive optics^{1,2} (AO) offers a real time compensation of the turbulence. The correction is however only partial^{1,3} and the long exposure images must be deconvolved to restore the fine details of the object.

A great care must be taken in the deconvolution process if one wants to obtain a reliable restoration with good photometric precision. Two aspects add to the difficulty: the fact that the residual point spread function (PSF) is usually not perfectly known,⁴⁻⁶ and the fact that astronomical objects are usually a mix of sharp structures and smooth areas. “MISTRAL” (Myopic Iterative STep Preserving ALgorithm)^{4,7} has been developed to account for these two points. It is based on a rigorous Bayesian approach which allows us to easily account for the noise in the image, the imprecise knowledge of the PSF, and the available *a priori* information on the object (spatial structure, positivity...). A specific edge preserving object prior is proposed, which is in particular well adapted for planetary-like objects.

The notion of AO partial correction is first discussed in Sect. 2. The needed image pre-processing are summarized in Sect. 3, then the principle of our deconvolution technique is briefly summarized in Sect. 4. In Sect. 5 the photometric accuracy of MISTRAL is first demonstrated on simulated AO images. The simulation parameters correspond to NAOS, the AO system of the VLT. MISTRAL is then applied to ADONIS images of Io taken at thermal wavelengths using the COMIC camera. This allows an accurate mapping of Io’s surface volcanic activity. We also used our deconvolution method on broad band filter (J,H,K) images of Uranus taken with SHARPII+ and on H band image of Neptune taken at CHFT with the “Hokupa’a” AO system. The structures of the rings and its innermost satellites have been successfully detected for Uranus, and fine structures are observed in Neptune clouds.

2. PARTIALLY CORRECTED AO IMAGES

Within the isoplanatic angle, the intensity $i(r)$ at the focal plane of the system consisting of the atmosphere, of the telescope and of the AO bench is given by:

$$i(r) = h(r) \star o(r) + n(r), \quad (1)$$

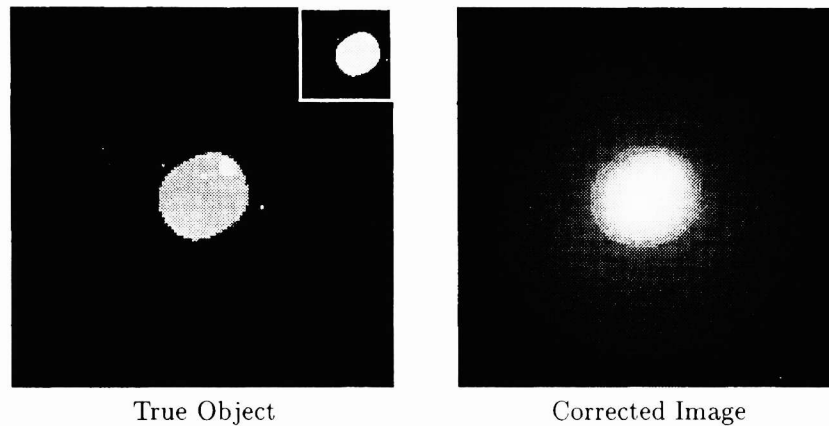


Figure 1. Planetary-type object ($M_v = 11$) and simulated VLT-NAOS image at $0.5 \mu m$ and for a 0.73 arcsec seeing. The Strehl Ratio (SR) is 2.1 %. The number of detected photons in the image is 10^8 photoe^- , the background noise has a $31 e^-$ standard deviation. The Field of View is 0.8 arcsec , $128 \times 128 \text{ pixel}$ image. The planetary disk is constituted of a uniform level plus a broad feature 10% brighter, and three small spots, 30% brighter. Four stars are added in the field with a 2.5 magnitude difference between the brightest and the faintest. The faintest corresponds to 40000 detected photons which corresponds to a maximum contribution of 155 photons/pixel in the image. The true object top-right display gives a log-scale representation.

where r is the spatial coordinate, $\mathbf{o}(r)$ is the observed object, $\mathbf{h}(r)$ is the system PSF and $\mathbf{n}(r)$ is an additive zero mean noise.

We consider here the case of AO corrected long exposure images. Such an image is presented in Fig. 1. In this numerical simulation we considered an 11th magnitude planetary-like object observed in the visible with the NAOS AO system⁸ installed on the VLT. This system will provide high performance in the near IR ($SR \approx 70\%$ at high flux). Here we consider the case of observations at visible wavelength ($\lambda = 0.5 \mu m$). In such conditions the image blur is very severe, the expected SR is only 2.1 % for a 0.73 arcsec seeing. Neither the fine structures on the surface of the object, nor the stars in the background, are apparent in the corrected image. A deconvolution is therefore required.

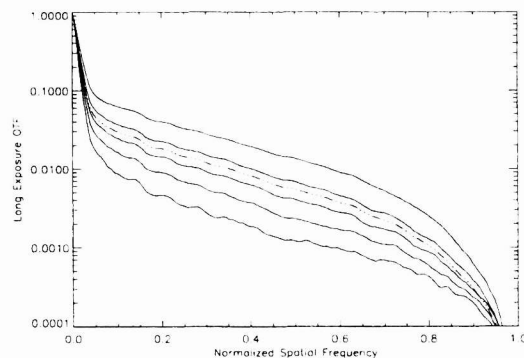


Figure 2. The OTFs are estimated for the following seeing values: from top to bottom, 0.65, 0.73, 0.79, 0.85 and 0.93 arcsec. The corresponding SRs are respectively: 3.8 %, 2.1 %, 1.3 %, 0.8 % and 0.4 % . The mean OTF is also drawn (dashed line)

The deconvolution procedure needs a measurement of the PSF. The usual procedure consists in recording the corrected image of a nearby unresolved star shortly after observing the object of interest. Since the correction quality depends on the observing conditions (turbulence strength, magnitude of the source used for wavefront sensing), the

unresolved star image is not a perfect measurement of the PSF associated with the image to be deconvolved.^{4,7,9} Actually the main source of PSF variability is the seeing fluctuation. The sensibility of the Optical Transfer Function (OTF) to the seeing variations is illustrated in Fig. 2. The OTFs are estimated for a seeing ranging from 0.65 to 0.93 arcsec. The corresponding SRs go from 3.7 % down to 0.4 %. The structure of the OTFs is typical of an AO corrected OTF^{10,3}: a low frequency lobe and a high frequency wing going up to the telescope cutoff frequency. The spatial frequencies between r_o/λ and D/λ , which would be lost without correction, are now preserved. The high frequency level is however low and very dependent of the seeing conditions. Here it changes by a factor of ten for rather realistic seeing changes.

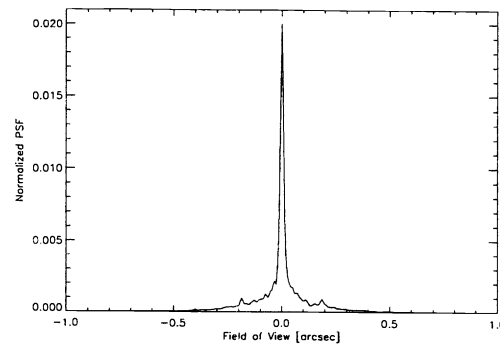


Figure 3. VLT-NAOS PSF at $0.5 \mu m$, for 0.73 arcsec seeing and a guide star magnitude $M_v = 11$. The PSF is normalized to its Strehl Ratio $SR \approx 2.1\%$.

The OTFs presented here derive from a careful study of the system performance.⁸ The corresponding PSF at 0.73 arcsec seeing is shown in Fig. 3. Note that despite the very low SR in the visible, a coherent peak is still clearly seen above the broad halo. This is characteristic of high order correction systems such as the VLT-NAOS one working in the visible: the residual phase variance is large due to the short wavelength, but the phase is mainly constituted of high order modes, hence the particular PSF profile. We will show in Sect. 5 that MISTRAL can restore high resolution maps out of these low SR visible VLT-NAOS images. Note that this suggests that the SR is not a good measurement of the image quality, when quality means “restorability”.¹¹

Of course the deconvolution can also be applied to IR images with more reasonable SRs as shown on ADONIS and HOKUPA’A data in Sect. 6. But we first recall the needed pre-processing data and the deconvolution approach in the following sections.

3. IMAGE PRE-PROCESSING

The typical raw data routinely acquired during an observing run are the images of the object of interest and the images of an unresolved star (to obtain a PSF estimation). Of course, these images must be pre-processed before any deconvolution in order to obtain images which are as close as possible to the convolution relation defined in Equation 1. The required pre-processing steps are:

- correction of the background and of the flat field,
 - correction of bad pixels,
 - correction of colored noise,
 - image conversion in photons (i.e multiplication by the camera gain),
 - estimation of the detector and background noises from background calibration and detector characteristics.
- Note that, if these data are not available, this estimation can be roughly made on the image itself assuming

zero mean gaussian statistics. In that case, the mean square root of the probability law can indeed be estimated on the negative pixels of the images

$$\sigma^2 = \frac{\pi}{2} \left(\langle \mathbf{i}(r) \rangle_{(r; \mathbf{i}(r) \leq 0)} \right)^2. \quad (2)$$

This σ^2 value is used for the noise estimation in the deconvolution process (see Equation 5)

4. DECONVOLUTION APPROACH

Most deconvolution techniques boil down to the minimization (or maximization) of a criterion. The first issue is the definition of a suitable criterion for the given inverse problem. The criteria presented here will be derived from a probabilistic approach. The second problem is then to find the position of the criterion's global minimum which is defined as the solution. In some cases it is given by an analytical expression, but most of the time one has to use an iterative numerical method to solve the problem.

In the following sections, we first consider the case of an assumedly known PSF, so-called “classical” deconvolution; the method is then extended to the joint estimation of the object and the PSF, called here “myopic” deconvolution.

4.1. Deconvolution with known PSF

Following a probabilistic approach, called maximum *a posteriori* [MAP],¹² the deconvolution problem can be stated as follows: we look for the most likely object \mathbf{o} given the observed image \mathbf{i} . This reads:

$$\hat{\mathbf{o}}_{\text{map}} = \arg \max_{\mathbf{o}} p(\mathbf{o}|\mathbf{i}) = \arg \max_{\mathbf{o}} p(\mathbf{i}|\mathbf{o}) \times p(\mathbf{o}) = \arg \min_{\mathbf{o}} [J_n(\mathbf{o}) + J_o(\mathbf{o})]. \quad (3)$$

The criterion to be minimized, $J = J_n + J_o$, is composed of a first term ($J_n = -\ln p(\mathbf{i}|\mathbf{o})$) accounting for the noise statistics in the image, plus a second term ($J_o = -\ln p(\mathbf{o})$) which allows to use the *a priori* knowledge we have on the object. This last term of course is a function of the type of object being observed. The choice of J_o for planetary type objects is discussed in the Sect. 4.1.2.

If no prior knowledge is available, one can still use the previous equations with $p(\mathbf{o}) = 1$. One therefore only maximizes $p(\mathbf{i}|\mathbf{o})$, also called likelihood of the data, to obtain a maximum likelihood solution. In this case the criterion is only constituted of the term J_n .

4.1.1. Maximum likelihood with photon noise

If the image is corrupted solely by photon noise, the maximum likelihood [ML] solution minimizes the following criterion, directly derived from the expression of Poisson statistics:

$$J_n^{\text{poisson}}(\mathbf{o}) = -\ln p(\mathbf{i}|\mathbf{o}) = \sum_r (\mathbf{h} \star \mathbf{o})(r) - \mathbf{i}(r) \ln[(\mathbf{h} \star \mathbf{o})(r)]. \quad (4)$$

The Richardson-Lucy algorithm [RL]^{13,14} is an iterative numerical method which converges towards the global minimum of J_{poisson} .

It is however well known that the restoration of the object using the sole data is an unstable process (see in particular Refs.¹⁵ and¹² for reviews). The noise is highly amplified in the solution. Of course, one can stop the RL before convergence to limit the noise amplification but in this case the solution is poorly defined. For sure, it is no more the minimum of any criterion. A better solution is to regularize the problem with an adequate object prior as proposed in Sect. 4.1.2.

4.1.2. Edge preserving regularized deconvolution

In the MISTRAL algorithm, we consider a white non stationary Gaussian noise in the image, which is a good approximation of a mix of photon and background (detector or sky-background) noise. Furthermore, the deconvolution is regularized by an object prior particularly adapted for planetary-like objects. This prior avoids the usual ringing artifacts¹⁶ given by standard deconvolution techniques on such sharp edge objects.^{17,4} The criterion to be minimized is:

$$J(\mathbf{o}) = J_n(\mathbf{o}) + J_o(\mathbf{o}) = \sum_r \frac{1}{2\sigma^2(r)} (\mathbf{i}(r) - (\mathbf{o} \star \mathbf{h})(r))^2 + J_o(\mathbf{o}), \quad (5)$$

where $\sigma^2(r) = \sigma_{ph}^2 + \sigma_{det}^2$ is the sum of the photon noise and the background noise variance. In the absence of background noise this expression of J_n is actually a first order development of Eq. 4. The regularization term is defined as:

$$J_o(\mathbf{o}) = \mu \sum_r \left[\left(\frac{\Delta \mathbf{o}(r)}{\delta} \right) - \ln \left(1 + \frac{\Delta \mathbf{o}(r)}{\delta} \right) \right], \quad (6)$$

where $\Delta \mathbf{o}(r) = \sqrt{\Delta_x \mathbf{o}(r)^2 + \Delta_y \mathbf{o}(r)^2}$, $\Delta_x \mathbf{o}$ and $\Delta_y \mathbf{o}$ are the object finite difference gradients along x and y respectively.

This regularization, called $L_1 - L_2$, is an isotropic version of the expression suggested by Brette.¹⁸ The global factor μ and the threshold δ have to be adjusted according to the noise level and the structure of the object. This is currently done by hand but an automatic procedure is under study.

We use a fast conjugate gradient method¹⁹ to minimize the global criterion J given in Eq. 5. This method is well adapted since the so-defined criterion is convex. An additional positivity constraint is used in MISTRAL, it is enforced with a reparameterization method ($\mathbf{o} = \mathbf{a}^2$)²⁰ where \mathbf{a} are the new parameters used in the minimization.

4.2. Myopic deconvolution

As mentioned in Sect. 2 the true residual PSF is seldom available. MISTRAL has the ability to estimate both the object and PSF from the image and some imprecise PSF measurement. The Eqs. 3 and 5 can indeed be generalized, in the same probabilistic framework, to the case of a joint estimation of $[\mathbf{o}, \mathbf{h}]$. One obtains:

$$[\hat{\mathbf{o}}, \hat{\mathbf{h}}] = \arg \max_{\mathbf{o}, \mathbf{h}} p(\mathbf{o}, \mathbf{h} | \mathbf{i}) = \arg \max_{\mathbf{o}, \mathbf{h}} p(\mathbf{i} | \mathbf{o}, \mathbf{h}) \times p(\mathbf{o}) \times p(\mathbf{h}) = \arg \min_{\mathbf{o}, \mathbf{h}} [J_n(\mathbf{o}, \mathbf{h}) + J_o(\mathbf{o}) + J_h(\mathbf{h})]. \quad (7)$$

The myopic criterion is given by Eqs. 5 and 6, now a function of \mathbf{o} and of \mathbf{h} , plus an additional term $J_h = -\ln p(\mathbf{h})$ which accounts for the knowledge, although partial, available on the PSF. Assuming stationary Gaussian statistics for the PSF, J_h reads:

$$J_h(\mathbf{h}) = \frac{1}{2} \sum_f \frac{|\tilde{\mathbf{h}}(f) - \tilde{\mathbf{h}}_m(f)|^2}{PSD_h(f)}, \quad (8)$$

where $\tilde{\mathbf{h}}_m = E[\tilde{\mathbf{h}}]$ is the mean OTF, and $PSD_h = E[|\tilde{\mathbf{h}}(f) - \tilde{\mathbf{h}}_m(f)|^2]$ is the associated spatial Power Spectral Density [PSD].

Such a regularization obviously ensures that the actual OTF is close to the mean OTF with respect to error bars given by the PSD, which characterizes the fluctuations around the mean. In practice, the mean PSF and the PSD are estimated by replacing, in their definitions, the expected values ($E[\cdot]$) by an average on the different images recorded on the unresolved star. Ideally one would want to estimate the PSF from the wavefront sensing data^{6,21} which would avoid the errors due to seeing fluctuations. But even in this case, the myopic approach can be interesting to account for the PSF uncertainties due to constant aberration calibration errors⁵ or to the wavefront sensing noise for faint stars.

Note that the new criterion is convex in \mathbf{o} for a given \mathbf{h} , convex in \mathbf{h} for a given \mathbf{o} but it is not convex on the whole parameter space. However it is possible to use starting points which are close to the global minimum, and we did not encounter minimization problems with the conjugate gradient method. A positivity constraint is also used on the PSF ($\mathbf{h} = \mathbf{b}^2$).

5. DECONVOLUTION OF SIMULATED VLT-NAOS IMAGES

The application of MISTRAL to the simulated VLT-NAOS visible image presented in Sect. 2 is discussed here.

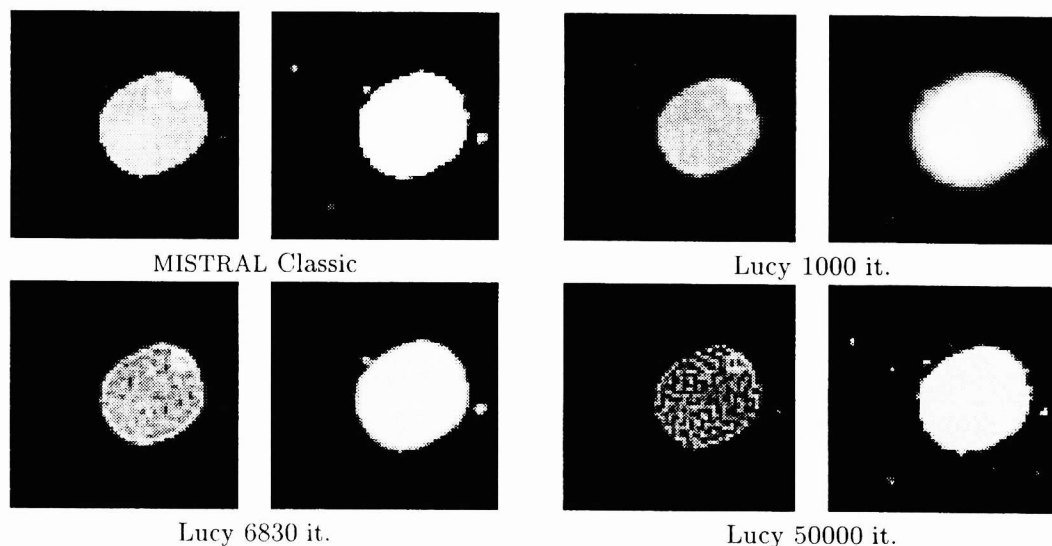


Figure 4. Classical deconvolution with MISTRAL and RL estimates with 1000, 6830 and 50000 iterations. The PSF is the true PSF. The deconvolution is performed on the 0.8 *arcsec* field of view but only a 0.4 *arcsec* sub-field is displayed. In each case we show the corresponding log-scale map. The distance to the true object is 5150 *photons/pixel* with MISTRAL and respectively 11800, 9900 and 13900 *photons/pixel* for the RL cases.

Fig. 4 shows the results obtained in the ideal case of a classical deconvolution using the true PSF. The deconvolution obtained with MISTRAL at convergence (360 iterations) of the minimization of Eq. 5 is compared to the RL estimation stopped respectively at 1000, 6830 and 50000 iterations. In each case a log-scale version of the restored object is shown in order to check the detection of the faint stars in the background.

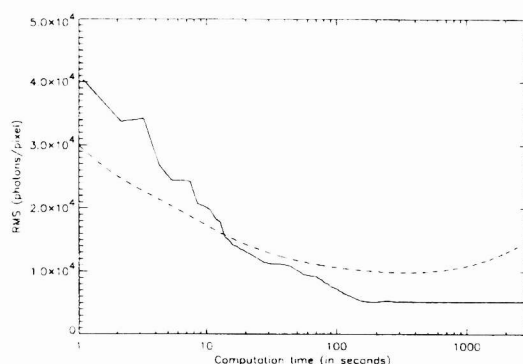


Figure 5. Distance to the true object, rms value expressed in photons/pixel, versus computation time: MISTRAL (solid line), RL (dashed line)

A quantitative measurement of the restoration quality can be given in terms of distance to the true object, rms value expressed in photons/pixel and computed on the full field of view. The distance is 5150 *photons/pixel* for the MISTRAL estimate, and respectively 11800, 9900 and 13900 *photons/pixel* for the RL cases. The evolution of the distance with the computation time is given in Fig. 5. The estimate obtained with 6830 iterations and shown in Fig. 4 therefore corresponds to the best RL estimate. The starting point is always the image thresholded to a slightly positive level for implementation of the positivity. The RL estimate never reaches the distance obtained with

MISTRAL and diverges for a large number of iterations. It goes from a low resolution estimate with ringing artifacts to a very noisy one. The restoration quality is obviously much higher with our regularized algorithm. The global photometry is very precisely restored. The stars in the background are well detected and only slightly smoothed. This large dynamic is permitted by a good model of the image noise. Note also that MISTRAL reaches convergence in a quite reasonable amount of time (≈ 390 s and 360 iterations), roughly the same time required for RL to reach its best estimation (≈ 330 s and 6800 iterations). Note also that MISTRAL is able to both restore the edge of the object and the structures on the surface.

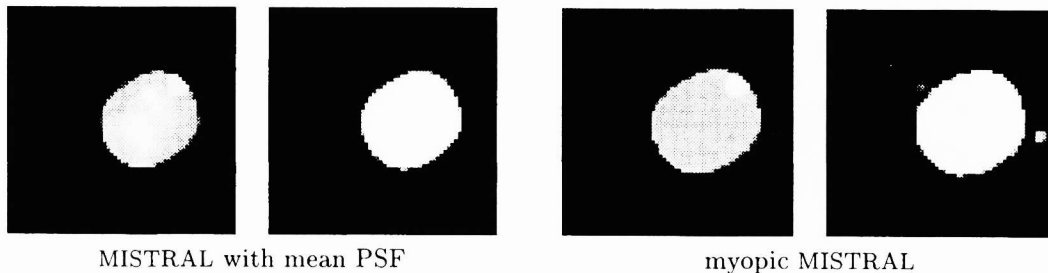


Figure 6. MISTRAL classical deconvolution with mean PSF considered as the true PSF and myopic deconvolution. In each case we show the corresponding log-scale map. The deconvolution is performed on the 0.8 arcsec field of view but only a 0.4 arcsec sub-field is displayed. The distance to the true object is respectively 23000 and 6800 photons/pixel.

We then consider the case of a poor estimation of the PSF. We recall that the image was obtained with a PSF corresponding to a 0.73 arcsec seeing. We assume that 5 images of an unresolved star were recorded shortly before or after. The seeing is supposed to be unstable and the seeing is actually 0.65 , 0.73 , 0.79 , 0.85 and 0.93 arcsec respectively for each of these calibration images. The OTF estimates are shown in Fig. 2 as well as the mean OTF. Since it can be difficult to estimate precisely the seeing conditions to select the correct OTF one may want to use a classical deconvolution assuming that the true OTF is the mean OTF. The result obtained with MISTRAL with this assumption is shown in Fig. 6. Despite the fact that the mean OTF is close to the true one ($SR = 1.7\%$ instead of 2.1%), the restoration is poor: artifacts on the surface, apparent diameter underestimated, no detection of the surrounding stars. The distance to the true object is large (≈ 23000 photons/pixel). The other approach is to use MISTRAL in the myopic mode (minimization at convergence of Eq. 7) with the same mean OTF and a PSD which is nothing but the variance estimated out these 5 OTF measurement for each spatial frequency. The restoration is very similar to that obtained with the true PSF. The distance to the true object is ≈ 6800 photons/pixel. Note however that part of the dynamic is lost. Only the two brightest stars are detected. The computation time required in the myopic case is ≈ 1900 s (1600 iterations) which is still quite reasonable.

6. DECONVOLUTION OF EXPERIMENTAL DATA

6.1. Monitoring of Io's volcanism

Io's volcanic activity, attributed to internal heating due to tidal effects between Jupiter and Io, was first discovered from space with Voyager 1 and 2 in 1979. They have shown the presence of active volcanic centers, called hot spots, detectable by their IR emission. Since then, and because of the increase in IR detector sensitivity, Io's variable volcanos of the Jupiter-facing hemisphere have been studied by ground-based observations when Io is located in the shadow of Jupiter.²² Since October 1996, ADONIS, the 52 actuators AO system mounted on the 3.6 m telescope of La Silla observatory, coupled with its COMIC thermal camera (CEA/LIR/LETI detector, 128×128 , 100 mas/pixel) has been used to monitor Io's volcanic activity.²³ Observations performed with a L' broad band filter ($\lambda_c = 3.8\mu\text{m}$) using the satellite itself as reference (angular size ~ 1.0 arcsec, $m_v \sim 5$) allow a complete mapping of its surface. In this spectral range the AO correction is quite efficient and the typical SR obtained is around 45% with a 0.8 arcsec seeing. An AO corrected image and the corresponding PSF are presented in Fig. 7. Only the bright Loki hot spot is detected on the AO corrected image. A deconvolution is required to study other structures. In addition to the residual blur, the image incorporates a rather uniform high level background emission produced by the sky and the

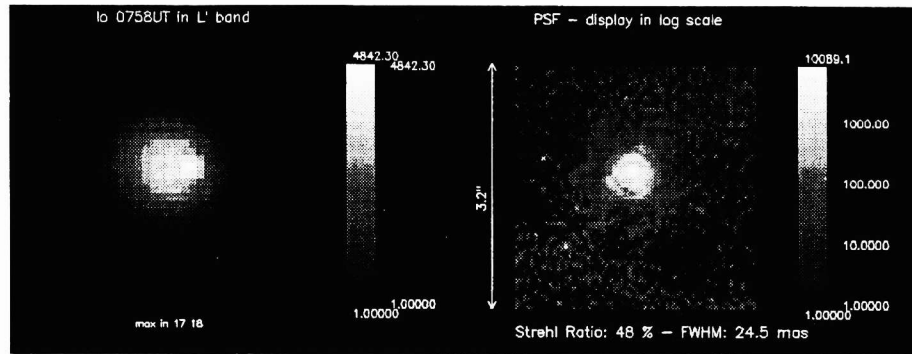


Figure 7. ADONIS image of Io and a log-scale representation of the corresponding PSF. Only the bright Loki hot spot is detected on the Io's disk.

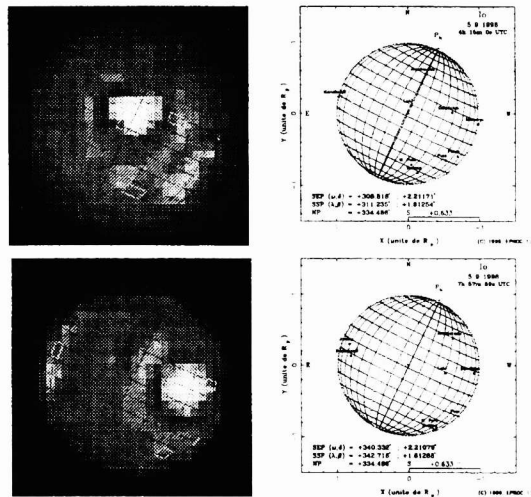


Figure 8. Two consecutive images of the Jupiter-facing hemisphere of Io observed with ADONIS/COMIC in L' band and processed with MISTRAL. The green boxes correspond to the projection of the hot spots detected by Galileo/NIMS during the first four orbits.²⁶ The right panel indicates the geometry of Io at the date of the observation and the name of the known hot spots (courtesy Bureau des longitudes)

bench optical elements²⁴ and a variable and inhomogeneous background modulated by the AO correction.²⁵ A good background subtraction is of course important for the deconvolution, and may be difficult to perform.

We present in Fig. 8 two consecutive images of Io's Jupiter-facing hemisphere taken in September 1998 and processed with MISTRAL.²⁷ We used the myopic mode to account for seeing variations. Loki, well-known hot spot located on the Jupiter-facing hemisphere, is quite active and surrounded by secondary outbursts. Pele-Pillan and Kanehikili volcanos are also detected. Standard deconvolution processes cannot be applied on these data. Indeed, in the absence of edge preserving regularization term, the whole energy of the disk tends to be concentrated in the bright Loki feature. Our observations are well correlated to and complement those made by Galileo/NIMS spectro-camera²⁶ (see Fig. 8). The coupling of AO system with a thermal camera and the use of a specific deconvolution process for planetary objects, such as MISTRAL, is very promising for our understanding of Io's volcanism which can only be accomplished by a frequent monitoring of its activity.

6.2. Study of the Uranian system

Uranus has been observed with broad band filters (J,H,K) using the SHARPII+ camera (Rockwell NICMOS3 detector, 1-2.5 μ m, 100 mas/pixel) and the ADONIS AO system, on May 2nd 1999. These observations have been performed thanks to the capability of the Shack-Hartmann WFS to analyze the wavefront on an extended object. Because of the relatively small angular size of the planet (3.5 arcsec) and the excellent seeing condition (0.5 arcsec and very stable), the correction quality was high and we got a SR of 48% in K band (2.2 μ m). The centroid position error, in each sub-pupil, is however higher on extended objects, hence a degraded AO performance on such extended objects. The image of an unresolved star is therefore a biased measurement of the PSF and a myopic deconvolution method is definitely necessary to restore the initial sharpness of the images. Figure 9 displays a set of data after

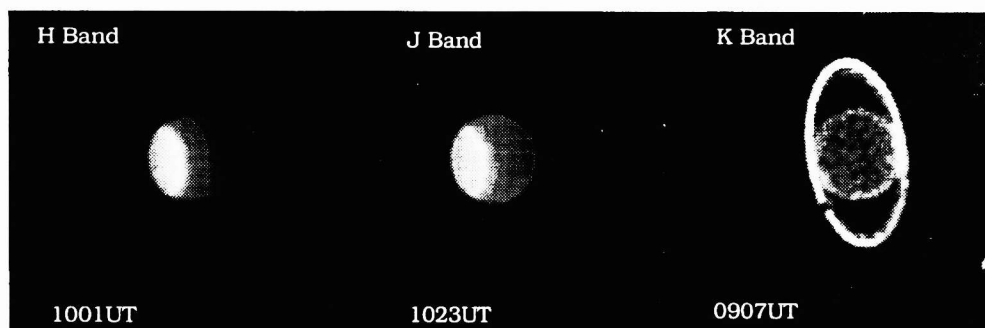


Figure 9. Uranus observed in May 1999 with ADONIS (north is down, east is left) and deconvolved by MISTRAL. In J and H bands, the hazy atmospheric regions are clearly visible around the pole. In K band, the methane atmospheric band absorbs the solar light and the bright feature observed is the Epsilon ring and its longitudinal anomaly.

deconvolution with MISTRAL. In J (1.2 μ) and H (1.6 μ m) bands, the planetary disk is not uniform as observed in the visible and shows bright polar haze distributed along a latitude. In K band, due to the methane atmospheric absorption band, the planet is dark and the brightest feature is the Epsilon ring with its longitudinal anomaly. Looking at the low intensity levels in J and H band (Fig. 10) one can see the Epsilon ring and also some innermost ones. The exterior satellites Ariel, Miranda and Puck can be detected with standard deconvolution such as RL. But the myopic deconvolution process also reveals the presence of the innermost satellites, Portia, Rosalind, Bianca and Juliet (see Fig. 10) which have been discovered by Voyager 2 in 1986 and never re-observed since then. After these first successful observations, the monitoring of Uranus and its environment will continue. The AO system facility and the accurate MISTRAL deconvolution method will allow us to study the atmospheric activity of the planets, the color and composition of the rings. The comparison of the positions of the faintest satellites with ephemerides will also better constrain physical parameters (body masses, flattening factor...) and to elaborate a more accurate analytical theory of the satellite motion.²⁸

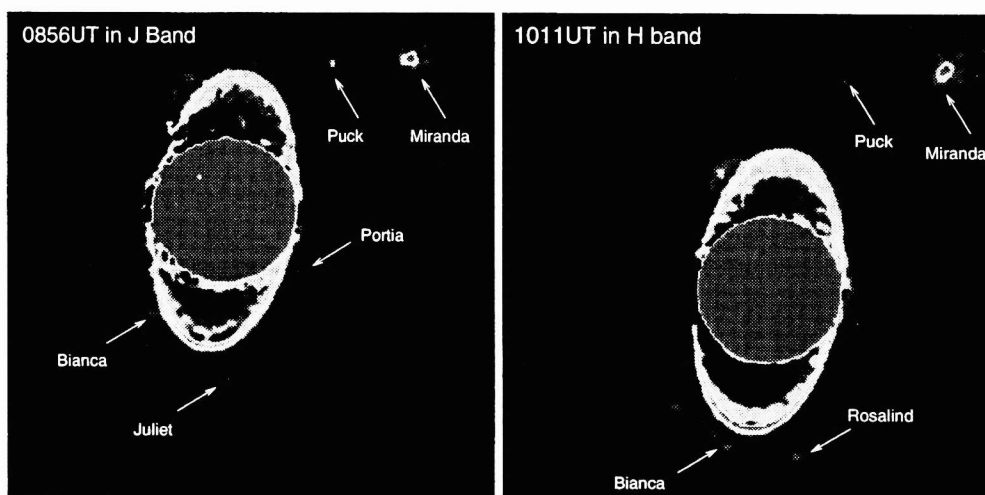


Figure 10. Logarithmic display of the MISTRAL images (north is up and east is left). Innermost rings and faintest satellites (first observed with Voyager in 1986) are also detected.

6.3. Study of the Neptune

The 36-actuator curvature AO system called “Hokupa’a” was used to observe Neptune at the CFHT both in November 1997 and in July 1998. It produced the first sharp infrared images of Neptune. These images show the fine structure of its cloud bands with high contrast, allowing the details of Neptune’s atmospheric activity to be observed from the ground for the first time.²⁹ Figure 11 shows images of Neptune obtained on July 6, 1998 in a methane absorption band ($1.72\ \mu\text{m}$), and deconvolved with the MISTRAL algorithm. At this wavelength Neptune’s atmosphere is very dark and high altitude clouds appear with a high contrast. The top three images are individual 600-second exposures taken at the time (UT) indicated above each image. Note how the fine structure in the cloud bands can be followed from one frame to another as the planet rotates. The upper left and right images have been numerically rotated about Neptune’s rotation axis to match the central image and co-added to it to form the bottom images, thus improving the signal-to-noise ratio. Intensity in the bottom right image has been increased to show fainter details. Particularly remarkable is the periodic pattern of bright dots seen just above the most southern cloud band (at the bottom of each image). Such a regular pattern of small clouds has never been observed before on Neptune and may be indicative of gravity waves in Neptune’s atmosphere. Adaptive optics followed by deconvolution with MISTRAL now allows us to monitor Neptune’s atmospheric activity in great detail from the ground.

7. CONCLUSION

MISTRAL is a myopic deconvolution algorithm particularly adapted for AO corrected images of astronomical objects. It accounts for the noise in the image, for the presence of sharp structures in the object and for the fact that the PSF is usually not perfectly known. Its ability to provide high photometric precision estimates with a quite reasonable computation time has been illustrated on simulated data. The simulation conditions correspond to a VLT-NAOS observation in the visible. Since the system is optimized in the near IR, the correction quality in the visible is low ($SR \approx 2\%$ here). Even in such a severe conditions a diffraction limited restoration is obtained.

MISTRAL has also been applied to ADONIS images of Io in the thermal domain and Uranus in the near IR and to HOKUPA’A images of Neptune in H band. In addition to the bright hot spot Loki, secondary outbursts were observed on Io’s Jupiter-facing hemisphere. Such observations are very promising for our understanding of Io’s volcanism which can only be accomplished by frequent monitoring of its activity. Concerning Uranus, the structures of the rings and its innermost satellites have been successfully detected. High altitude clouds of Neptune are also studied. And the high contrast brought by the deconvolution allows the observation of fine structures. We will continue a monitoring of Uranus and Neptune. Solar system studies (atmospheric activity of the planets, color and composition of the rings, position of the faint satellites) require high resolution and high photometric precision data. This can be obtained with large telescope AO observations in conjunction with a high precision deconvolution technique.

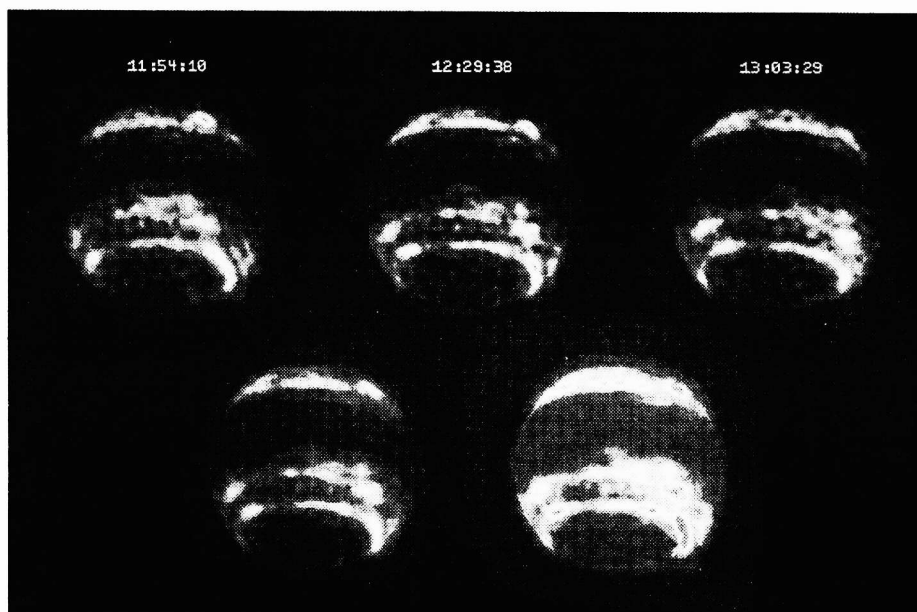


Figure 11. False-color images of Neptune obtain at CHFT with “Hokupa’a” AO system on July 6, 1998 in a methane absorption band ($1.72\ \mu\text{m}$) and deconvolved by MISTRAL. The top three images are individual 600-second exposures taken at 11:54:10, 12:29:38 and 13:03:29 UT time. Note how the fine structure in the cloud bands can be followed from one frame to another as the planet rotates. These left and right images have been numerically rotated about Neptune’s rotation axis to match the central image and co-added to it to form the bottom images, thus improving the signal to noise ratio. Intensity in the bottom right image has been decreased to show fainter details.

8. ACKNOWLEDGMENTS

The authors thank Gérard Rousset, Vincent Michau, Jérôme Idier, Amandine Blanc and Guy Le Besnerais for many fruitful discussions. We are indebted to ESO-3.6m support team, in particular the Telescope Operators for their assistance during these difficult and unusual planetary object observations.

REFERENCES

1. G. Rousset, J.-C. Fontanella, P. Kern, P. Gigan, F. Rigaut, P. Léna, C. Boyer, P. Jagourel, J.-P. Gaffard, and F. Merkle, “First diffraction-limited astronomical images with adaptive optics,” *Astron. Astrophys.* **230**, pp. 29–32, 1990.
2. F. Roddier, ed., *Adaptive Optics in Astronomy*, Cambridge University Press, 1999.
3. J. M. Conan, P. Y. Madec, and G. Rousset, “Image formation in adaptive optics partial correction,” in *Active and Adaptive Optics*, ICO, (Garching, Germany), 1993.
4. J.-M. Conan, T. Fusco, L. Mugnier, E. Kersalé, and V. Michau, “Deconvolution of adaptive optics images with imprecise knowledge of the point spread function: results on astronomical objects,” in *Astronomy with adaptive optics: present results and future programs*, ESO/OSA, (Sonthofen), Sept. 1998.
5. T. Fusco, J.-P. Véran, J.-M. Conan, and L. Mugnier, “Myopic deconvolution method for adaptive optics images of stellar fields,” *Astron. Astrophys. Suppl. Ser.* **134**, pp. 1–10, Jan. 1999.
6. J.-P. Véran, F. Rigaut, H. Maître, and D. Rouan, “Estimation of the adaptive optics long exposure point spread function using control loop data,” *J. Opt. Soc. Am. A* **14**(11), pp. 3057–3069, 1997.
7. J.-M. Conan, L. M. Mugnier, T. Fusco, V. Michau, and G. Rousset, “Myopic deconvolution of adaptive optics images using object and point spread function power spectra,” *Appl. Opt.* **37**, pp. 4614–4622, July 1998.

8. G. Rousset, F. Lacombe, P. Puget, N. Hubin, E. Gendron, J.-M. Conan, P. Kern, P.-Y. Madec, D. Rabaud, D. Mouillet, A.-M. Lagrange, and F. Rigaut, "Design of the Nasmyth Adaptive Optics System (NAOS) of the VLT," in *Astronomical Telescopes & Instrumentation*, D. Bonaccini and R. K. Tyson, eds., vol. 3353, Proc. Soc. Photo-Opt. Instrum. Eng., (Kona, Hawaii), Mar. 1998.
9. J. C. Christou, "Deconvolution of adaptive optics images," in *ESO/OSA topical meeting on astronomy with adaptive optics present results and future programs*, ESO/OSA, 1998.
10. M. C. Roggemann and C. L. Matson, "Power spectrum and Fourier phase spectrum estimation by using fully and partially compensating adaptive optics and bispectrum postprocessing," *J. Opt. Soc. Am. A* **9**(9), pp. 1525–1535, 1992.
11. J.-M. Conan, *Étude de la correction partielle en optique adaptative*. PhD thesis, Université Paris XI Orsay, Oct. 1994.
12. G. Demoment, "Image reconstruction and restoration: Overview of common estimation structures and problems," *IEEE Trans. Acoust. Speech Signal Process.* **37**, pp. 2024–2036, Dec. 1989.
13. W. H. Richardson, "Bayesian-based iterative method of image restoration," *J. Opt. Soc. Am.* **62**(1), pp. 55–59, 1972.
14. L. B. Lucy, "An iterative technique for rectification of observed distributions," *Astrophys. J.* **79**(6), pp. 745–754, 1974.
15. D. M. Titterton, "General structure of regularization procedures in image reconstruction," *Astron. Astrophys.* **144**, pp. 381–387, 1985.
16. J.-P. Véran, *Estimation de la réponse impulsionnelle et restauration d'image en optique adaptative Application au système d'optique adaptative du Télescope Canada-France-Hawaii*. PhD thesis, Ecole Nationale Supérieure des Télécommunications, Nov. 1997.
17. L. M. Mugnier, J.-M. Conan, T. Fusco, and V. Michau, "Joint maximum a posteriori estimation of object and PSF for turbulence degraded images," in *Bayesian Inference for Inverse problems*, vol. 3459, pp. 50–61, Proc. Soc. Photo-Opt. Instrum. Eng., (San Diego, CA (USA)), July 1998.
18. S. Brette and J. Idier, "Optimized single site update algorithms for image deblurring," in *Proceedings of the International Conference on Image Processing*, pp. 65–68, IEEE, (Lausanne, Switzerland), 1996.
19. Groupe Problèmes Inverses, "Gpav : une grande œuvre collective," internal report, Laboratoire des Signaux et Systèmes, CNRS/Supélec/Université Paris-Sud, 1997.
20. E. Thiébaud and J.-M. Conan, "Strict *a priori* constraints for maximum-likelihood blind deconvolution," *J. Opt. Soc. Am. A* **12**(3), pp. 485–492, 1995.
21. S. Harder, *Reconstruction de la réponse impulsionnelle du système d'optique adaptative ADONIS à partir des mesures de son analyseur de surface d'onde et Étude photométrique de la variabilité des étoiles YY Orionis*. PhD thesis, Université Joseph Fourier, Grenoble 1, May 1999.
22. J. R. Spencer, J. A. Stansberry, C. Dumas, D. Vakil, R. Piegler, M. Hicks, and K. Hege, "History of high-temperature Io volcanism: February 1995 to may 1997," *Geophys. Res. Lett.* **24**, p. 2451, 1997.
23. F. Marchis, R. Prangé, and J. C. Christou, "Adaptive optics mapping of io's volcanism in the thermal ir," *Icarus*, 1999. submitted.
24. D. Le Mignant, E. Gendron, and F. Marchis, "The eso ADONIS adaptive optics system: Study of the 3–5 μ m background emissivity," in *ESO conference and workshop proceeding*, vol. 56, p. 575, OSA/ESO, (Garching, Germany), 1998.
25. H. Geoffray, "Thermal background blurring on ADONIS system," in *ESO conference and workshop proceeding*, vol. 56, p. 531, OSA/ESO, (Garching, Germany), 1998.
26. R. Lopes-Gautier, A. Davies, R. Carlson, W. Smythe, L. Kamp, L. Soderblom, F. E. Leader, and R. Mehlman, "Hot spots on Io: Initial results from Galileo's near infrared mapping spectrometer," *Geophys. Res. Lett.* **24**, p. 2439, 1997.
27. R. Prangé, F. Marchis, and T. Fusco, "Mapping and monitoring of Io's hot spots by use of the ESO adaptive optics system," in *31st Annual Meeting of the DPS*, (Padova, Italy), Oct. 1999.
28. F. Marchis, J. Berthier, P. Descamps, T. Fusco, R. Prangé, and T. Sekiguchi, "Ground-based high resolution observations of the Uranian system in the near IR," in *31st Annual Meeting of the DPS*, (Padova, Italy), Oct. 1999.
29. F. Roddier, C. Roddier, J. E. Graves, N. M. J., and O. T., "Neptune cloud structure and activity: Ground based monitoring with adaptive optics," *Icarus* **136**, pp. 168–172, 1998.